Supporting Information

Direct CO_2-to-CO Conversion with H_2O on an In_2O_3 Photocatalyst Enabled by Atomically Precise Pd Sites

Fengyang Yu,* Cheng Chang, Hanghang Kang, Huixian Ma, Wansheng Zong* and Lina Su*

Abstract: Utilizing a MOF-templated strategy, we constructed a single-atom Pd-anchored In_2O_3 nanotube photocatalyst. The Pd sites promote the generation and migration of photogenerated carriers, thereby enabling highly selective CO_2 reduction with water vapor, leading to a CO production rate 10 times higher than that of pristine In_2O_3.

Table of Contents

1. Experimental Section

Chemicals and Reagents

All chemicals were purchased from commercial suppliers and used without further purification. These include indium(III) nitrate hydrate ($In(NO_3)_3 \cdot xH_2O$, >99.9%), terephthalic acid (H_2BDC, >98%), and palladium(II) acetate (Pd content: 47%).

Synthesis of MIL-68(In)

A solution of $In(NO_3)_3 \cdot xH_2O$ (4.082 g) in DMF (50 mL) was combined with H_2BDC (2 g) and stirred for 35 min. The mixture was transferred into a 100 mL Teflon-lined autoclave and heated at 110 °C for 24 h. The resulting white solid was collected by centrifugation, washed thoroughly with methanol, and dried at 70 °C overnight.

Synthesis of In_2O_3/Pd Catalysts

MIL-68(In) (2 g) and specific quantities of palladium(II) acetate (1.48, 7.4, 14.8 mg) were dissolved in methanol (30 mL) via sonication for 10 min, followed by stirring for 15 min at room temperature. The solvent was evaporated at 60 °C under stirring, and the resulting solid was calcined in a muffle furnace at 500 °C for 5 h in static air with a ramp rate of 2 °C·min^{-1}.

Photocatalytic CO_2 Reduction

The reaction was conducted in a gas–solid phase system (PLR-MFPR-1). A catalyst layer was prepared by uniformly depositing 5 mg of photocatalyst onto a glass slide (2.5 × 3.5 cm), which was then placed in a quartz reactor. After injecting 0.2 mL of ultrapure water, the reactor was sealed, purged with high-purity CO_2, and pressurized to 200 kPa. The reaction was initiated under irradiation from a 300 W Xe lamp (light intensity: ~220 mW·cm^{-2}). Gaseous products (CO and CH_4) were analyzed using a gas chromatograph (GC-2002) equipped with an FID detector and an argon carrier gas, with the column maintained at 60 °C.

Photoelectrochemical Measurements

The working electrode was prepared by coating a slurry of catalyst (5 mg in 1 mL ethanol) onto an ITO substrate and drying in air. Measurements were performed in a three-electrode system with the ITO electrode as the working electrode, an Ag/AgCl reference electrode, and a Pt counter electrode in 0.1 M Na_2SO_4 electrolyte. EIS was measured at the open-circuit potential from 100 kHz to 0.1 Hz. Transient photocurrents were recorded at 0 V vs. Ag/AgCl over six light–dark cycles (10 s each).

Apparent Quantum Efficiency (AQE)

Apparent Quantum Efficiency (AQE) is defined as the ratio of the number of electrons involved in the reaction to the number of incident photons. Typically, the production of one CO molecule requires two electrons. AQE is measured using the following formula:

$$AQE(\%) = \frac{(2 \times N_A \times N_{CO}) \times (h \times c)}{I \times A \times \lambda \times t} \times 100\%$$

Where, N(CO) is number of CO (mole) evolved in time "t" (1h), N_A is Avogadro's number (N = 6.022 × 10^{23} mol^{-1}), I is the incident solar irradiance (I = 81.7 mW·cm^{-2}), "A" is the coated area of the catalyst was 8.75 cm^2. λ refers to the specific wavelengths used in this study (420 nm), "h" is Planck's constant (6.62 × 10^{-34} J·s), and "c" is the speed of light in a vacuum (3.0 × 10^8 m·s^{-1}).

Material Characterization

XRD patterns were recorded on a Bruker D8 Advance diffractometer with Cu Kα radiation (λ = 1.5418 Å), scanning 2θ from 10° to 80°.SEM images were obtained on a Hitachi SU8220, and TEM/STEM analysis was performed on a JEOL JEM-F200 (200 kV). Atomic-resolution HAADF-STEM and EDX mapping were conducted on a JEOL ARM 200F equipped with a spherical aberration corrector and a large-solid-angle EDX detector. XPS spectra were acquired on a Thermo Scientific K-Alpha+ spectrometer with an Al Kα source, and binding energies were calibrated against C 1s at 284.80 eV. UV-Vis diffuse reflectance spectra were measured on a Shimadzu UV-3900 using $BaSO_4$ as a reference. Pd content was determined by ICP-OES (Agilent 5110).

In Situ DRIFTS under Light Irradiation

The sample mixed with KBr was pressed into a cell. Spectra were collected on a Bruker INVENIO FTIR spectrometer with an MCT detector. After Ar purging, the reaction was initiated under Xe lamp irradiation with humidified CO_2 flow. Spectra (4000–740 cm^{-1}) were recorded every 5 min at a resolution of 4 cm^{-1} (16 scans per spectrum).

XAFS Measurements and Analysis

Pd K-edge XAFS data were collected at the BL14W1 beamline of SSRF (Shanghai) in fluorescence mode using a Si(111) monochromator. Samples were pelletized and measured at room temperature. Reference spectra of Pd foil and PdO were acquired under the same

conditions. Data processing and fitting were performed using the Athena and Artemis software packages.The acquired EXAFS data was processed via Athena module implemented in the Demeter software. The k^2 weighted EXAFS were obtained by subtracting the pre-edge and post-edge background from the overall absorption and then normalized with respect to the edge jump step in 1st derivative line. EXAFS of the Pd foil is fitted and the obtained amplitude reduction factor S02 value was set in the EXAFS analysis to determine the coordination numbers (CNs) in scattering path in sample. Subsequently, the (k) data was then Fourier transformed to R space, using a hanning window (dk=1 Å-1) to separate EXAFS conditions from different coordination shells. XAFS fitting was proceeded using ARTEMS software. The EXAFS equation was listed:

$$\chi(k) = \sum_j \frac{N_j S_0^2 F_j(k)}{kR_j^2} exp[-2k^2\sigma_j^2] e^{-2R_j/\lambda_j(k)} sin[2kR_j + \phi_j(k)]$$

S_0^2 is the amplitude reduction factor, $F_j(k)$ is the effective curved-wave backscattering amplitude, N_j is the number of neighbors in the jth atomic shell, R_j is the distance between the X-ray absorbing central atom and the atoms in the *j*th atomic shell, λ_i is the mean free path in *Å*, *j(k)* is the phase shift (including the phase shift for each shell and the total central atom phase shift), *j* is the Debye-Waller parameter of the *j*th atomic shell(variation of distances around the average R_j). The relevant parameters were calculated with the ab initio code FEFF.The k^2 weighting were used for the fitting of Pd samples. For samples, the parameters, coordination number, bond length, and E_0 shift (C_N, R, ΔE_0) were fixed, while the Debye-Waller factor (σ^2) was set. The Wavelet transformed (WT) of EXAFS was performed via Wtexafs software. The parameters were listed as follows: *R* range, 1-4 *Å*, k range, 0 - 12 $Å^{-1}$ for samples; k weight, 2; and Morlet function with κ=10, σ=1 was used as the mother wavelet to provide the overall distribution.

Density Functional Theory (DFT) Calculations

All density functional theory (DFT) calculations were performed using the Vienna ab initio Simulation Package (VASP 5.3). The supercell model was constructed via Material Studio (MS), with a 20 Å vacuum layer set along the surface normal direction to suppress periodic interactions. The calculations adopted the Perdew-Burke-Ernzerhof (PBE) functional within the generalized gradient approximation (GGA) and the projector-augmented wave ultrasoft pseudopotentials (PAW-USP). The plane-wave cutoff energy was set to 520 eV, and the Brillouin zone sampling was performed using a 3×3×1 Monkhorst-Pack k-point grid. During the geometric optimization, the bottom-layer atoms were fixed, with the convergence criteria set as a total energy change less than 10^{-4} eV and a maximum atomic force of 0.02 eV·$Å^{-1}$. The adsorption energy ($\Delta E_a d_s$) was calculated according to Equation: $\Delta E_{ads} = E_{tot} - E_{small} - E_{ini}$. where E_{tot} refers to the total energy of the adsorption model of a single molecule or molecular mixture on the photocatalyst, E_{small} denotes the energy of a single molecule or the total energy of a molecular mixture in the adsorption model, and E_{ini} represents the total energy of the pristine photocatalyst model.

2. Supplementary Figures

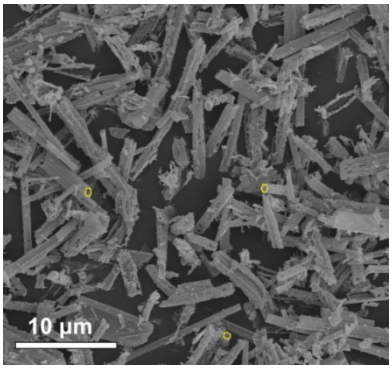

Figure S1. SEM images of In_2O_3/Pd.

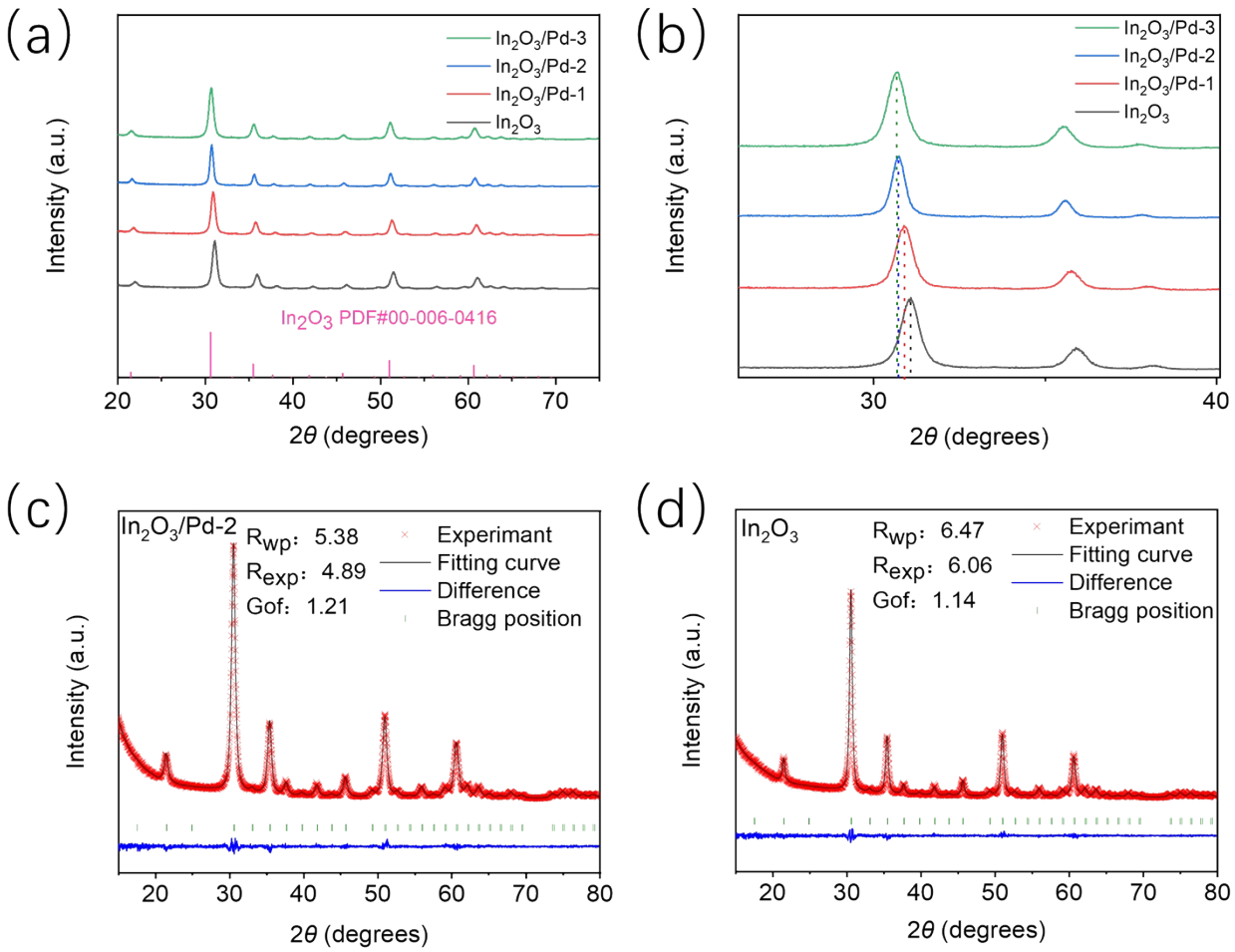

Figure S2. (a, b) XRD patterns of In_2O_3, and In_2O_3/Pd-2. (c) Rietveld refinement XRD pattern of pure In_2O_3/Pd-2. (d) Rietveld refinement XRD pattern of In_2O_3.

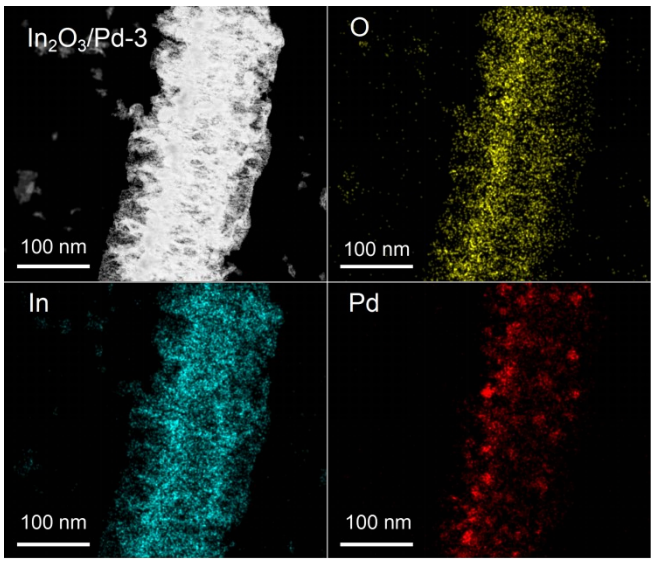

Figure S3. EDX mapping of In_2O_3/Pd-3.

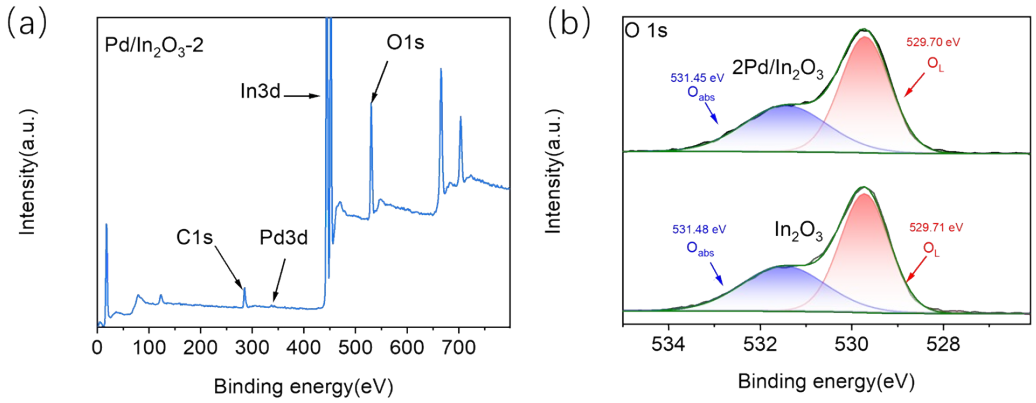

Figure S4. (a) XPS survey spectra of In_2O_3/Pd. (b) O 1s XPS spectrum of In_2O_3 and In_2O_3/Pd-2.

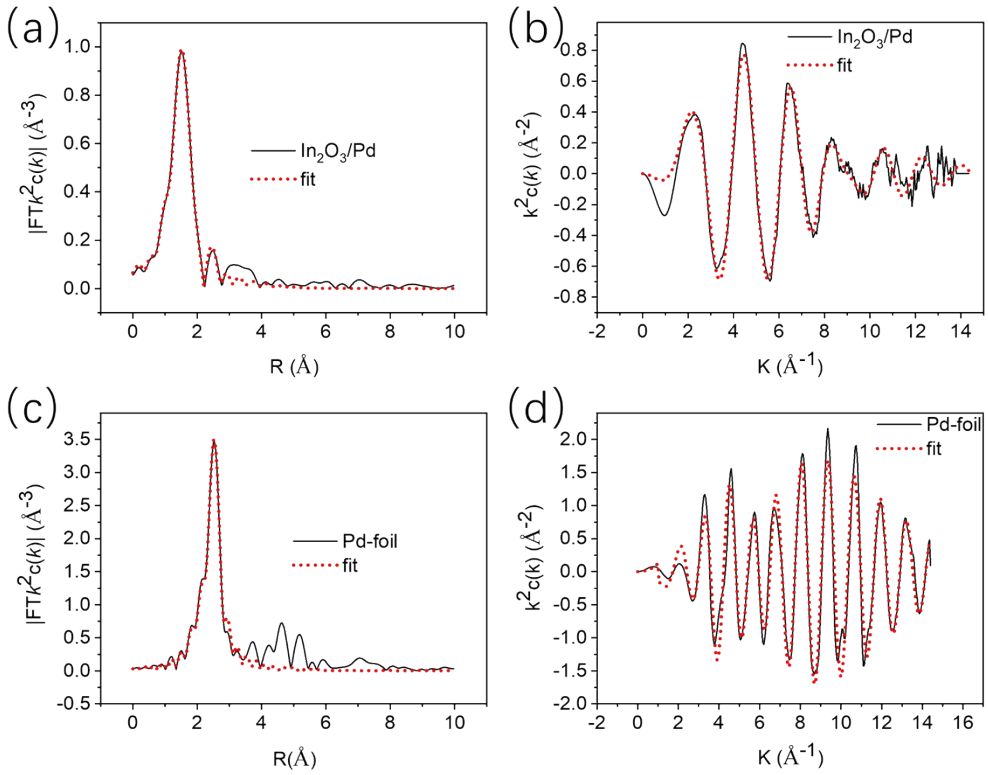

Figure S5. (a) EXAFS R space of In_2O_3/Pd-2. (b) EXAFS k-space of In_2O_3/Pd-2. (c) EXAFS R space of Pd-foil. (d) EXAFS k-space of Pd-foil.

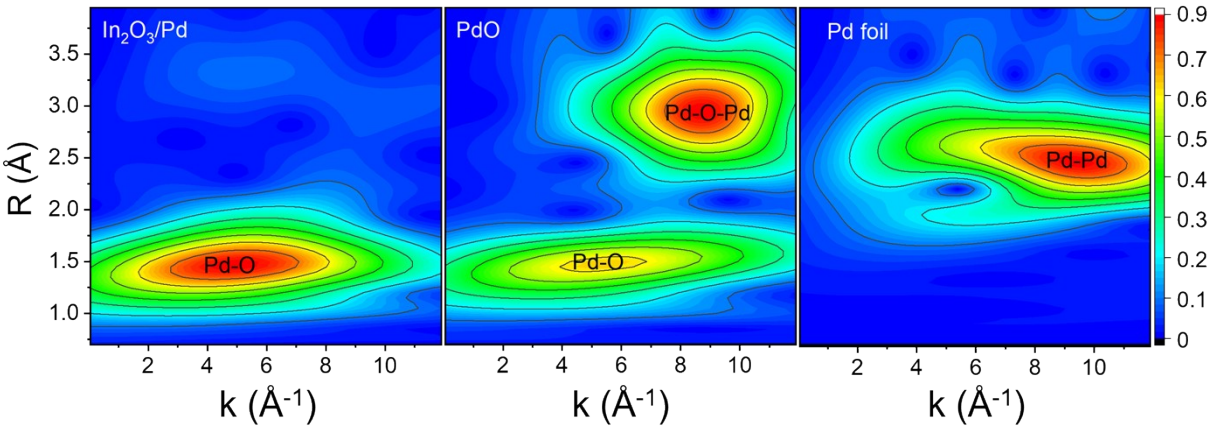

Figure S6. WT EXAFS image of In_2O_3/Pd-2, PdO and Pd foil.

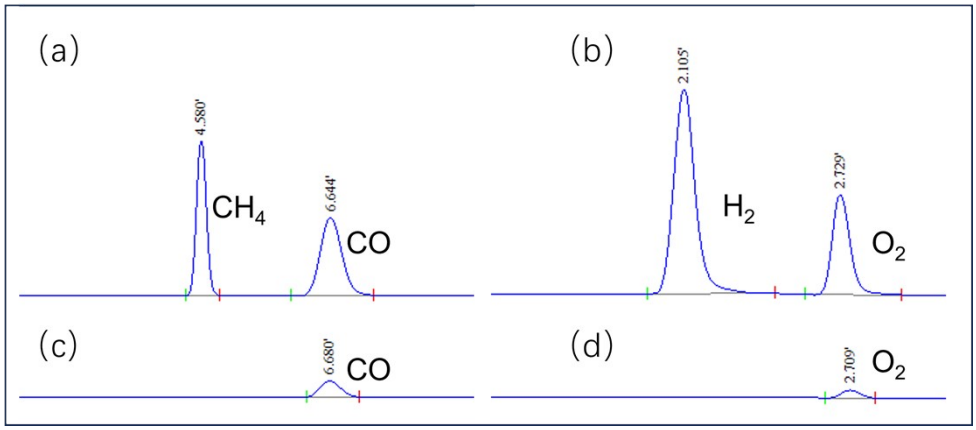

Figure S7. Gas chromatography (GC) analysis of: (a) CH_4/CO mixed standard gas, (b) H_2/O_2 mixed standard gas, and (c, d) catalytic reaction products.

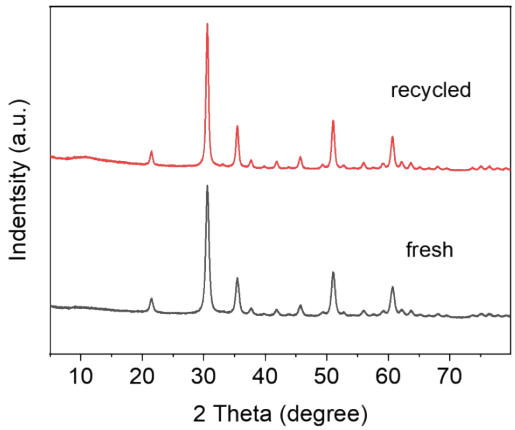

Figure S8. XRD patterns of In_2O_3/Pd-2 catalysts before reaction and after stability test.

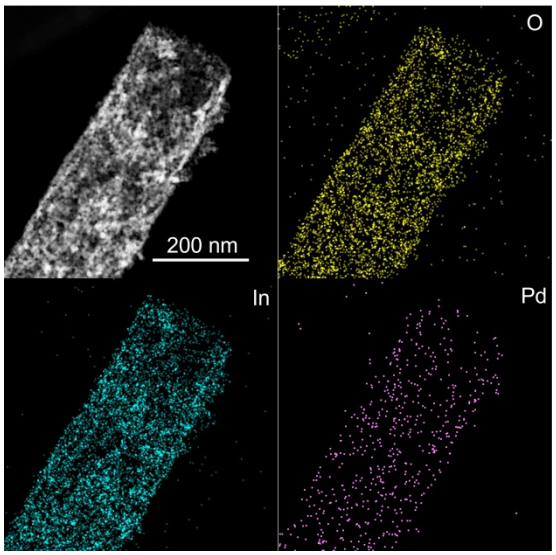

Figure S9. TEM image and selected area energy dispersive X-ray elemental mapping spectroscopy (EDS) of after stability test in In_2O_3/Pd-2.

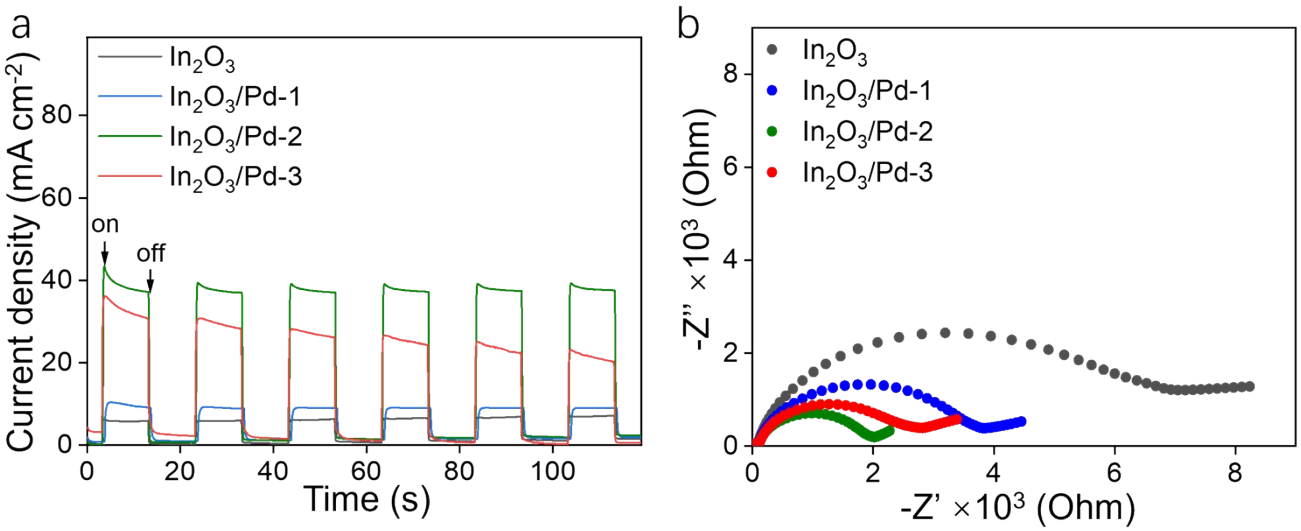

Figure S10. (a) Photocurrent response and (b) ESI of In_2O_3, In_2O_3/Pd-x (x=1-3).

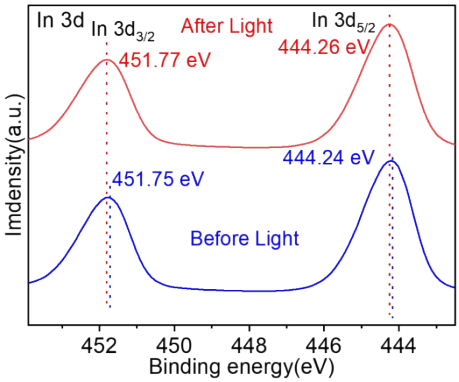

Figure S11. In situ XPS spectra of high-resolution In 3d of In_2O_3/Pd-2.

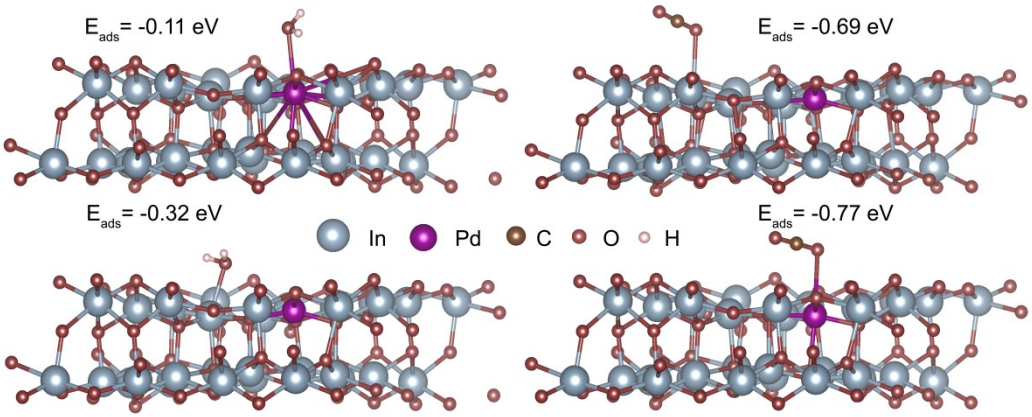

Figure S12. The adsorption energy of CO_2 and H_2O on the surface of In_2O_3/Pd-2.

3. Supplementary Tables

Table S1. The contents of Pd atom in the samples according to ICP-OES methods.

Sample	ICP-OES (%)
In_2O_3/Pd-1	0.1
In_2O_3/Pd-2	0.5
In_2O_3/Pd-3	1.0

Table S2. EXAFS fitting parameters at the Pd K-edge for various samples. (S_0^2=0.82)

Sample	Shell	CN[a]	R(Å)[b]	σ2(Å²)[c]	ΔE0(eV)[d]	R factor
Pd foil	Pd-Pd	12*	2.74±0.01	0.0057	4.0±0.4	0.0037
In_2O_3/Pd-2	Pd-O	3.9±0.1	1.50±0.01	0.0050	0.5±1.4	0.0041
	Pd-O-In	1.3±0.3	2.51±0.02	0.0001		
	Pd-In	0.2±0.1	2.74±0.05	0.0035		

[a]*N*: coordination numbers; [b]*R*: bond distance; [c]σ^2: Debye-Waller factors; [d] ΔE_0: the inner potential correction. *R* factor: goodness of fit.

Table S3. Comparison of the photocatalytic performance of reported photocatalysts for CO_2 conversion into CO productions in pure water.

Catalysts	**Light sources**	**Yield ($\mu mol \cdot g^{-1} \cdot h^{-1}$)**	**Selectivity (%)**	**refs**
$BiOI/Bi_2O_2CO_3$	300 W xenon lamp	8.11	90	[1]
Bi_4NbO_8Cl/ $Bi_5Nb_3O_{15}$	300 W xenon lamp(>400nm）	3.19	79.1	[2]
11CN	300W xenon lamp	2.13	100	[3]
$BiOCl/In_2O_3$	300 W Xe lamp	6.9	100	[4]
$Cu_2Cl(OH)_3/In/In_2O_3$	300 W Xe lamp	4.36	80	[5]
Ag/GaOOH/CTO	100 W Hg lamp	11.1	95	[6]
ZnO_{ss}	300W xenon lamp	6.7	80	[7]
Ag_3BiI_6	300W xenon lamp (AM 1.5G)	0.23	69.7	[8]
Ti3-MOF-74.	300 W xenon lamp (>420nm）	13.1	100	[9]
5% CuCN	300 W xenon lamp (>420nm）	14.65	100	[10]
In_2O_3/Bi_2S_3	300 W Xe lamp	2.67	100	[11]
$Cd_{0.96}Ni_{0.04}S/Mn:In_2O_3$	300 W Xe lamp	14.47	100	[12]
CPB/IO-2	300 W Xe lamp AM 1.5	12.5	76.36	[13]
Cu/TiO_2-3	300 W Xe lamp	15.27	100	[14]
$2Pd/In_2O_3$	**300W xenon lamp**	**9.22**	**100**	**This work**

References

[1] Z. Wang, B. Cao, R. Li, B. Jing, X. Cai, J. Cao, D. He and Y. Xu, *J. Alloys Compd.*, 2025, 182207.

[2] X. Tian, X. Wang, F. Li, P. R. Makgwane, Y. Yao and X. Liu, *J. Environ Chem.l Eng.*, 2025: 119708.

[3] D. Hu, S. Li, Y. Chen, Y. Shen, X. Liao, X. Zhou, H. Xu, Y. Tan and J. Zhong, *Int. J. Hydrogen Energy,* 2025, **158:** 150571.

[4] X. Liu, H. Zhang, X. Qiu, H. Ye, Y. Xie and Y. Ling, *Appl. Catal. A Gen.*, 2024, **671:** 119574.

[5] H. Zhang, Z. Fan, H. Ye, Y. Xie and X. Liu, *J. Mol. Struct.*, 2024, **1310:** 138281

[6] H. Qiu, A. Yamamoto, H. Yoshida, *Sustain. Energy Fuels*, 2024, **8(6):** 1287-1294.

[7] X. He, X. Li, L. Zhang, Z. Wang, J. Ma, *Ind. Crops Prod.*, 2024, **214:** 118530.

[8] J. Chang, T. Lin, K. C. Hsiao, K. P. Chiang, Y. H. Chang and M. Wu, *Adv. Sci.*, 2024, **11(24):** 2309526.

[9] Z. Ding, X. Tang, D. Zhao, S. Yan, L. Li, P. Li, W. Tang, S. Zhang and Y. Zeng, *Inorg. Chem.*, 2024, **63(30):** 14193-14199.

[10] L. Wang, J. Li, C. Zhong, C. He, M. Khan, D. Liu, J. Wang, R. Yang, M. Kan, L. Wang, S. Wu and J. Zhang, *Small*, 2025, **21(27):** 2503390

[11] M. Sun, K. Fan, C. Liu, T. Gui, C. Dai, Y. Jia, X. Liu and C. Zeng, *Langmuir*, 2024, **40(24):** 12681-12688.

[12] Y. Xu, T. Han, T. Ji, W. Luan, R. Zhao, J. Han and L. Wang, *Int. J. of Hydrogen Energy*, 2024, **59:** 299-305.

[13] J. Ding, X. Deng, J. Fan, Y. Wang, Z. Li and Q. Liang, *Inorg. Chem.*, 2023, **62(40):** 16493-16502.

[14] K. Zhu, Q. Zhu, M. Jiang, Y. Zhang, Z. Shao, Z. Geng, X. Wang, H. Zeng, W. Zhang, K. Huang and S. Feng, *Angew. Chem. Int. Ed.*, 2022, **61(34):** e202207600.